

We are IntechOpen, the world's leading publisher of Open Access books Built by scientists, for scientists

6,900

Open access books available

186,000

International authors and editors

200M

Downloads

Our authors are among the

154

Countries delivered to

TOP 1%

most cited scientists

12.2%

Contributors from top 500 universities



WEB OF SCIENCE™

Selection of our books indexed in the Book Citation Index
in Web of Science™ Core Collection (BKCI)

Interested in publishing with us?
Contact book.department@intechopen.com

Numbers displayed above are based on latest data collected.
For more information visit www.intechopen.com



Cretaceous Research: A New Constraint on the Paleostress Regime of Southwest Japan Based on Microfabric Analysis of a Granitic Pluton

Yasuto Itoh

Additional information is available at the end of the chapter

<http://dx.doi.org/10.5772/67357>

Abstract

Origin of a conspicuous microscopic fabric of a granitic pluton in the eastern part of southwest Japan, which has been an autochthonous component of the East Asian margin since the late Mesozoic, was elucidated through well-organized rock magnetic and geochronological investigations. The voluminous Late Cretaceous Toki Granite suffered a thermochemical event succeeding to its emplacement, which resulted in tightly grouped principal axes of the anisotropy of magnetic susceptibility (AMS). The magnetic fabrics originate from ferromagnetic and paramagnetic minerals precipitated upon the surface of fractures developed under regional tectonic stress. Together with previous studies of three-dimensional microcrack generation and intrusion sequence of dike swarms in the Toki Granite, temporal changes in the azimuths of AMS principal axes delineate a drastic shift in tectonic stress regime along the Asian continental margin from the Late Cretaceous to the Paleocene. This remarkable event is probably linked to a regional unconformity contemporaneously formed on the convergent margin.

Keywords: paleostress, rock magnetism, anisotropy of magnetic susceptibility, fracture, tectonics

1. Introduction

For years, measurements of the anisotropy of magnetic susceptibility (AMS) have been applied to granitic rocks to determine their primary microfabric, a characteristic that reflects the azimuth of their original viscous emplacement flow (e.g., [1]). Their incompetence to strain means in general that the original fabrics are readily preserved [2]. On the other hand, AMS fabric has often been used to indicate the orientation of fractures developed after the initial emplacement of granitic plutons. For example, Itoh and Amano [3] executed an elaborate rock magnetic study on a plutonic body and found that granite samples adjacent to a large fault are remag-

netized, and that their anisotropy forms an oblate shape nearly parallel to the azimuth of the fault plane. Based on microscopic observation, they confirmed the presence of fine authigenic particles of iron oxides within fault-related veins, which undoubtedly contribute to the conspicuous AMS fabric. Another notable point among their paleomagnetic results is that nested blocks of plutons had suffered differential rotation bounded by numerous orthogonal fractures.

Uplift and cooling of a granitoid body result, in general, in fracture formation influenced by intragranular microscale cracking of quartz grains [4], which develops because quartz undergoes stronger thermal contraction than feldspar. The regional stress field regime controls the formation of intrinsic microcracks whose orientations are normal to the orthogonal principal stress axes. It is conceivable that the network of cracks normal to the minimum axis is the most open and permeable pathway of formation fluids. Thus, the AMS fabric, which originates from ferromagnetic minerals precipitating on the fracture surface, mimics the paleo-stress field. The author attempts in this case study to verify the reliability of AMS data as a stress indicator by analyzing underground samples free from secondary weathering effects.

2. Geological settings

Analytical samples used in the present rock magnetic study were taken from the Mizunami underground research laboratory (abbreviated as MIU; see **Figure 1**) of the Japan Atomic Energy Agency (JAEA). It is an underground laboratory that tests the in situ stability of the upper crust, which consists, around the MIU, of a Jurassic to Cretaceous accretionary complex, Cretaceous to Paleogene volcano-plutonic complex, Miocene marine sediments and Miocene to Pliocene nonmarine clastics in ascending order [5, 6]. In the MIU's main and ventilation shafts, the base of the sedimentary units was confirmed at 166.27 m and 168.67 m below the surface, and the downside comprises a pluton of Toki Granite.

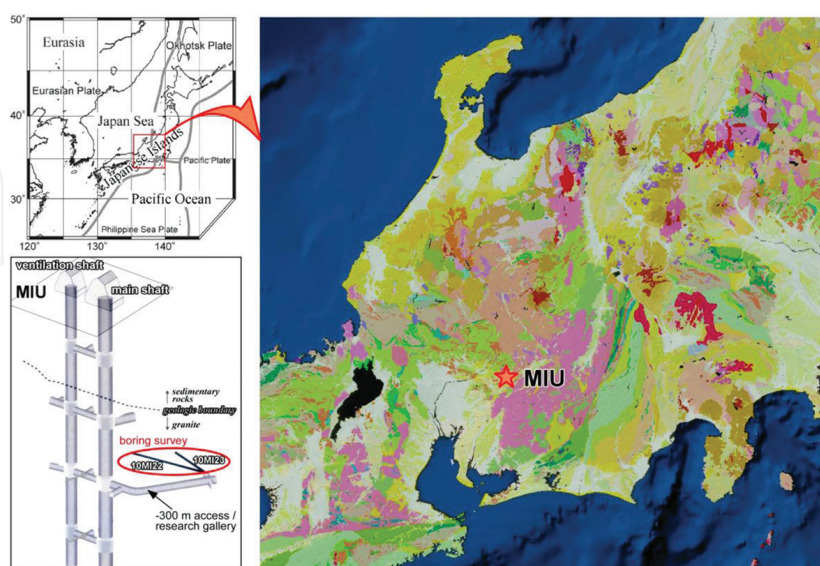


Figure 1. Index maps of the study drilling site (MIU: Mizunami underground research laboratory). The geologic map is after [5].

Toki Granite is one of the Late Cretaceous granitoids extensively distributed in southwest Japan. The pluton has yielded a CHIME monazite age of 68.3 ± 1.8 Ma [7] and whole-rock Rb-Sr ages of 72.3 ± 3.9 Ma [8] and 68.2 ± 1.1 Ma [9]. It is a stock, 14 km \times 12 km in areal extent [10], having a vertical thickness of at least 1.5 km based on borehole investigations by JAEA.

3. Paleo-/rock magnetism

3.1. Sampling and methods

Paleo-/rock magnetic sampling was executed on core samples from a research borehole (10MI22) drilled horizontally from the 300-m level access/research gallery (**Figure 1**). **Figure 2** shows the lithology column and fracture density along the borehole. We obtained fresh granites from six sites (MI2201 ~ 05, 07), dark-colored aphyric intrusive rocks from two sites (MI2209, 10) and greenish altered granites from two sites (MI2206, 08). The intrusive body is closely associated with the main fault observed in the drift. Altered samples MI2206 and MI2208 are located in a fracture zone and in the alteration halo of the intrusion, respectively. Conventionally drilled core samples were successfully oriented on the basis of the correlation between fractures on the core surface and the side-wall images for the cored interval obtained by a borehole television (BTV). **Figure 3** shows typical examples of fractured core photo (a) and BTV image of the side-wall (b).

Ten to eighteen standard-sized cylindrical specimens (25 mm diameter, 22 mm long) were taken from 10 points along the Toki Granite core. Bulk initial magnetic susceptibility was measured for all the specimens using a Bartington susceptibility meter (MS2). We conducted progressive thermal demagnetization (PThD) testing on selected specimen from each site. Natural remanent magnetization (NRM) was measured using a cryogenic magnetometer (760-R SRM, 2-G Enterprises) within a magnetically shielded room at Kyoto University and spinner magnetometers (SMM-85, Natsuhara-Giken; SSM-1A, Schonstedt Instrument) at Osaka Prefecture University. The PThD test was performed, up to 680°C in air, using a non-inductively wound electric furnace with an internal residual magnetic field less than 10 nT.

3.2. Basic sample properties

For the fresh granites, we found semistable components to have a converging trend on origin of the vector-demagnetization diagrams across a broad distribution of unblocking temperatures (T_{UB}) up to 580°C after the northerly component was demagnetized at around 300°C, whereas the altered granites were highly unstable during PThD treatment, and the magnetic components of most of the specimens were not isolated. On the other hand, we successfully identified the converging trend on origin of the vector-demagnetization diagrams and isolated stable magnetic components with a broad distribution of T_{UB} up to 680°C for the intrusive rocks. The directions of the characteristic remanent magnetization (ChRM) were calculated using a three-dimensional least squares analysis technique after [11].

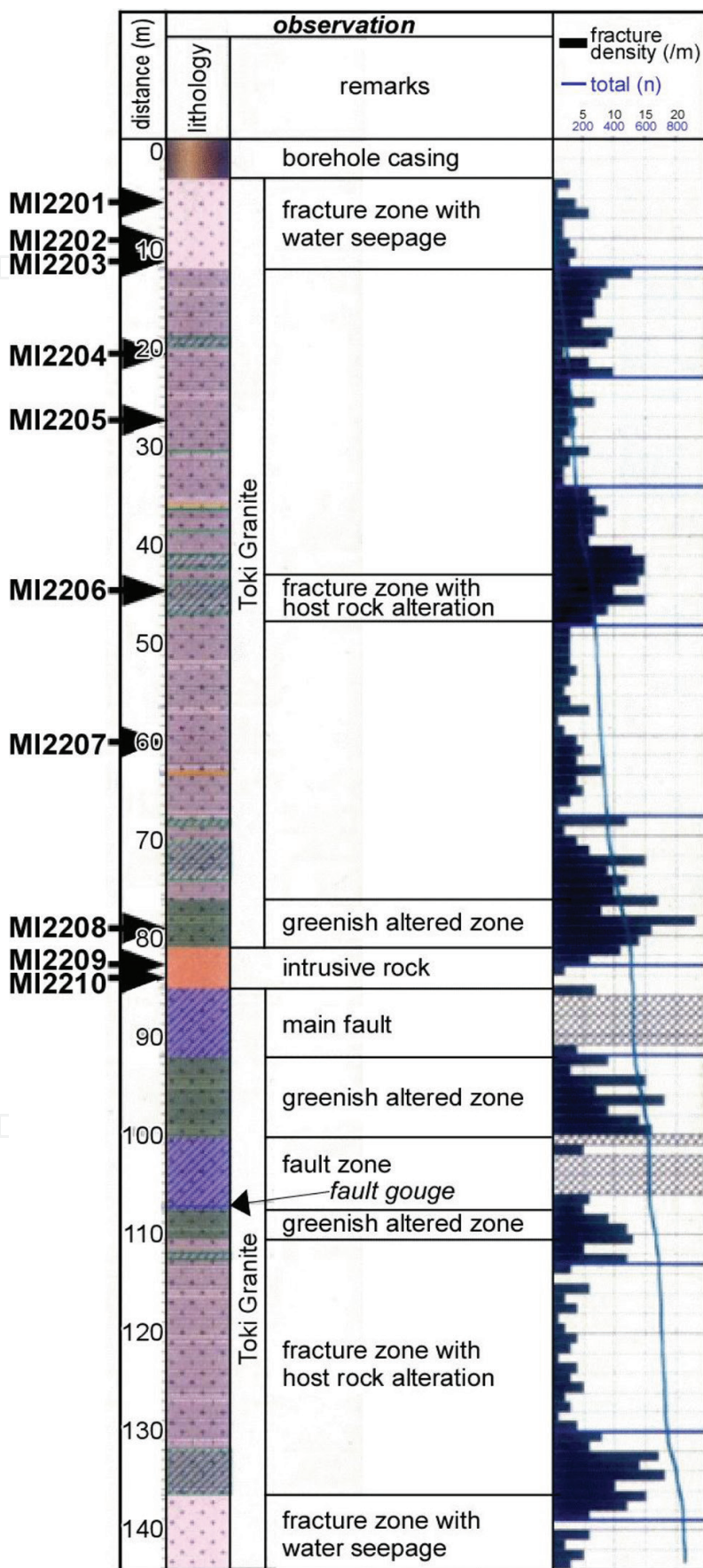


Figure 2. Columnar section of the 10MI22 borehole with rock magnetic sampling horizons.

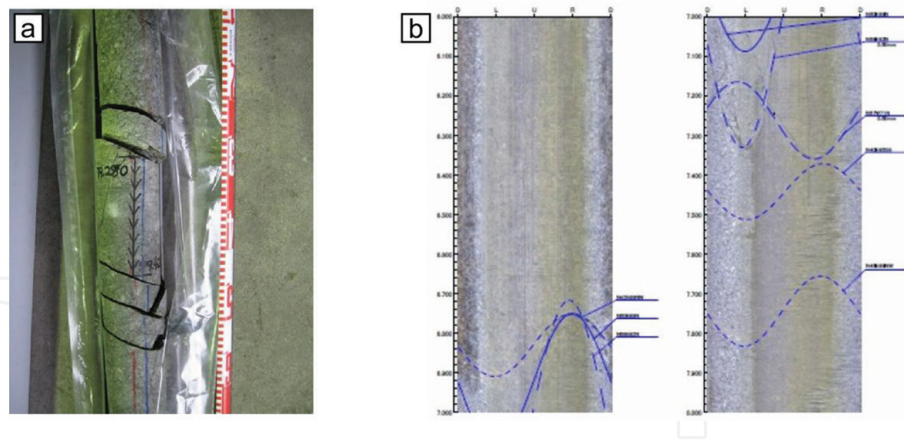


Figure 3. Determination of the orientation of conventionally drilled core samples. Fractures in a core (a) and side-wall images obtained by a borehole television (BTV; b) were correlated.

Site-mean ChRM directions in geographic coordinates are presented in **Figure 4**. As mentioned above, altered granites were thermally unstable, and number of data points was too small to obtain statistical parameters. It should be noted that the remanence directions of the fresh granites show a large scatter even in a single site. Based on thermochronological analysis, Sasao et al. [12] showed incipient rapid cooling of the Toki Granite and argued that the considerable dispersion of paleomagnetic directions in the intact rock may be attributed to plastic deformation of granites during the cooling period. The diversity of the magnetic properties of the samples may originate from thermochemical changes after the pluton was emplaced because the significantly weak NRM of the altered rocks (**Figure 5**) imply leaching of iron oxide. Decreases in bulk initial susceptibility and increases in the frequency dependence (the F factor defined by [13]) of altered rocks (**Figure 6**) indicate a loss of magnetic carrier and smaller magnetic particles, respectively. The author attempts to identify ferromagnetic minerals in the following sections.

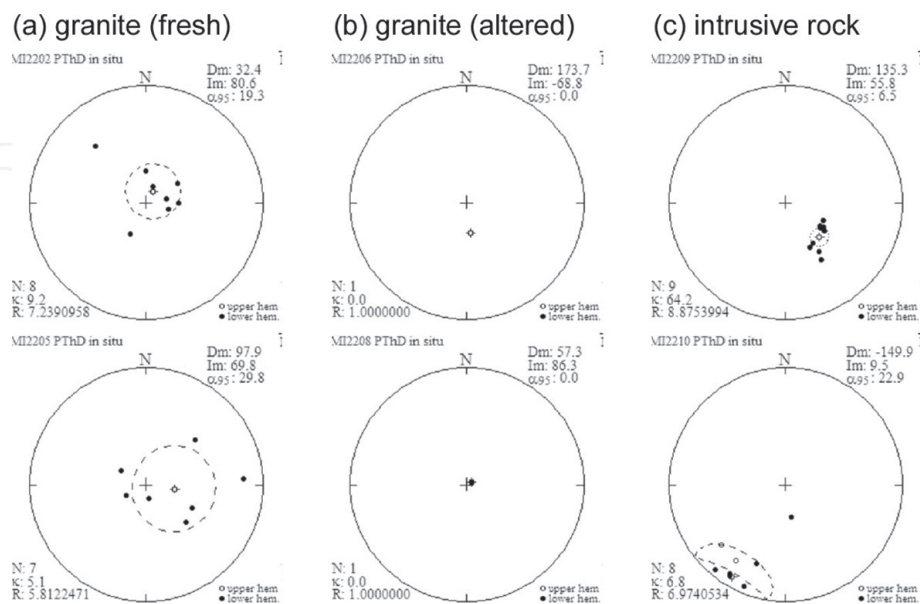


Figure 4. Equal-area projections of site-mean magnetic directions obtained from core samples of fresh granite (a), altered granite (b) and intrusive rock (c) along the 10MI22 borehole. Solid and open symbols are data plotted on the lower and upper hemispheres, respectively. Dotted ovals show 95% confidence limits.

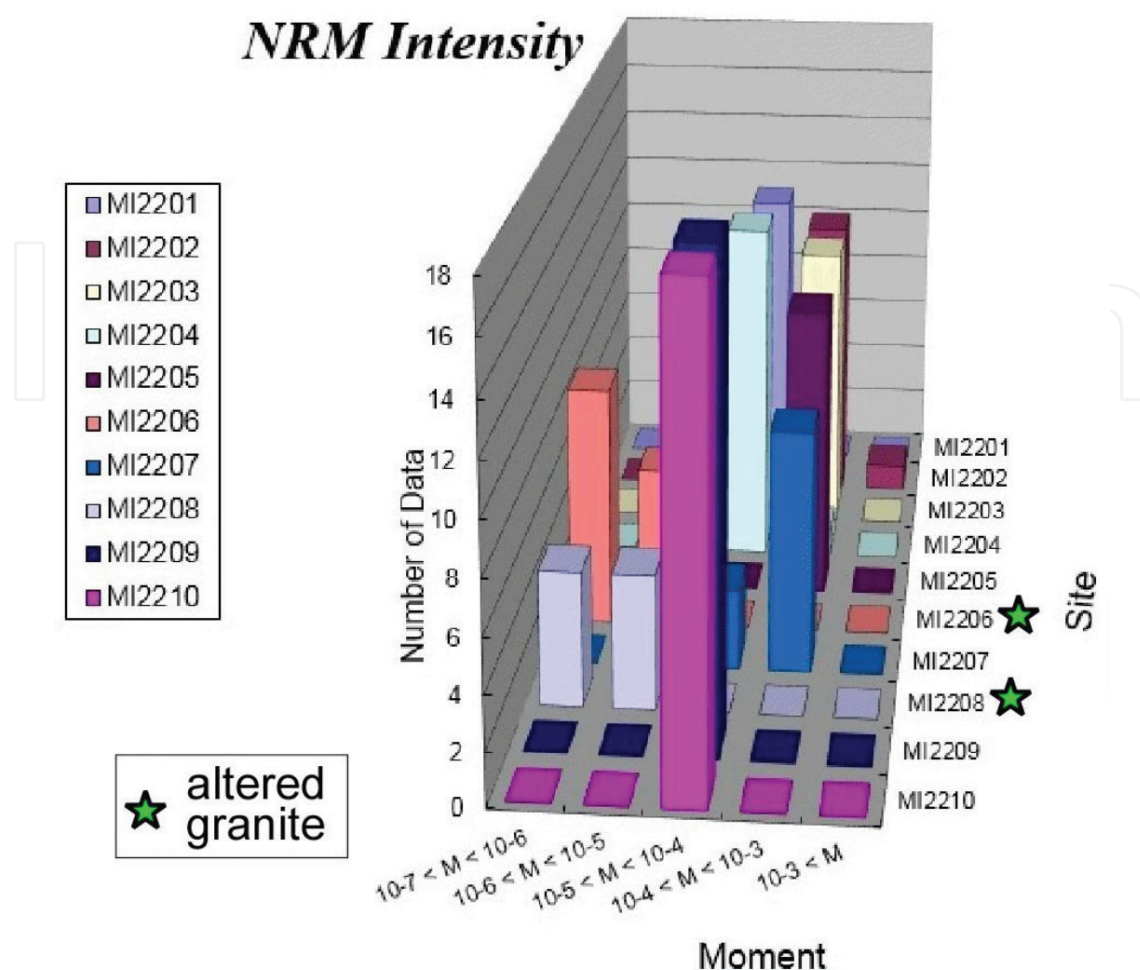


Figure 5. Comparison of intensities of natural remanent magnetization (NRM) of core samples of the 10MI22 borehole.

3.3. Hysteresis properties

Magnetic hysteresis parameters were determined with an alternating gradient magnetometer (MicroMag 2900, Princeton Measurements Corporation) at Kyoto University. Samples from 10 sites were gently ground in a mortar. From the ground material, 50 rock chips as large as 1 mm were randomly selected from each site. In addition, portions of the powder (about 50 mg) were wrapped in plastic film to prepare 50 samples per site. Because felsic minerals are more resistant to the grinding process, they tend to be concentrated in the chip samples, whereas the more fragile mafic minerals tend to concentrate in the powder samples. Among the 10 sites, magnetization of the intrusive rocks did not reach saturation at the highest field of the apparatus, so they were then excluded from the following analysis.

Figure 7 presents correlation plots of hysteresis parameters, namely, J_{rs}/J_s versus H_{cr}/H_c [14], using values of the coercivity of remanence (H_{cr}) obtained through backfield demagnetization experiments. Trends a, b and c originate from synthetic and crushed natural

magnetite [15], single-domain (SD) and multidomain (MD) mixtures of magnetite [16] and superparamagnetic (SP) and SD mixtures of magnetite [17, 18], respectively. As for the fresh granites (1), most of the data are found around mixture trends of various sizes of magnetite, implying that the effect of secondary mineral precipitation remains minimal. A small number of chip samples are plotted between trends for SD and MD mixtures of magnetite (b) and SP and SD mixtures of magnetite (c), suggesting differences in grain-size distribution. Data for the altered granite (2) fall completely separate from the SD and MD mixture trend and imply dominance of finer grains. The logarithmic parameters of chip data resemble data for remagnetized limestones, whose remanence is carried by authigenic magnetite having negligible shape anisotropy [17].

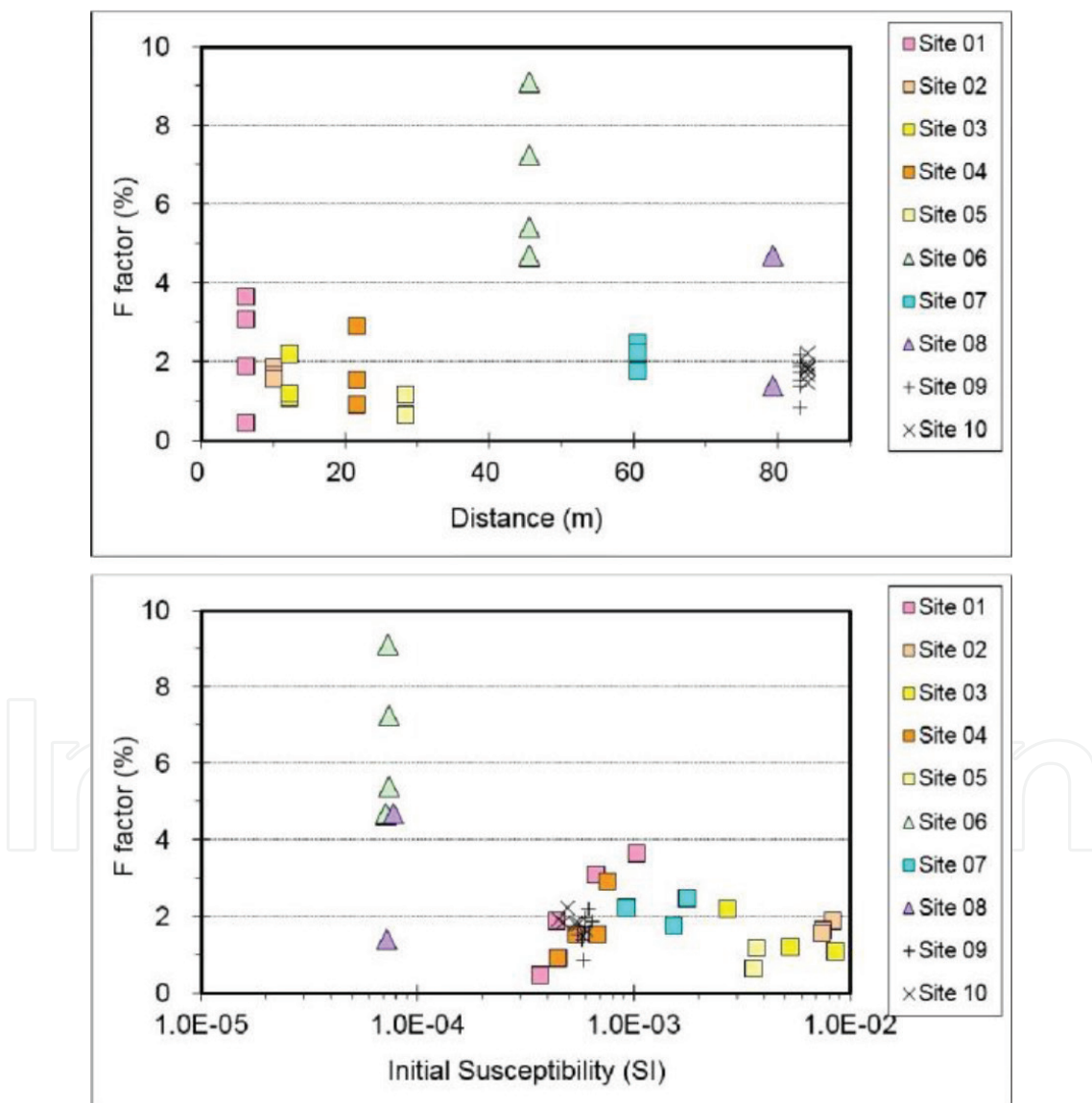


Figure 6. F-factor plots for core samples of the 10MI22 borehole. Symbol: square = fresh granite, triangle = altered granite, cross = intrusive rock.

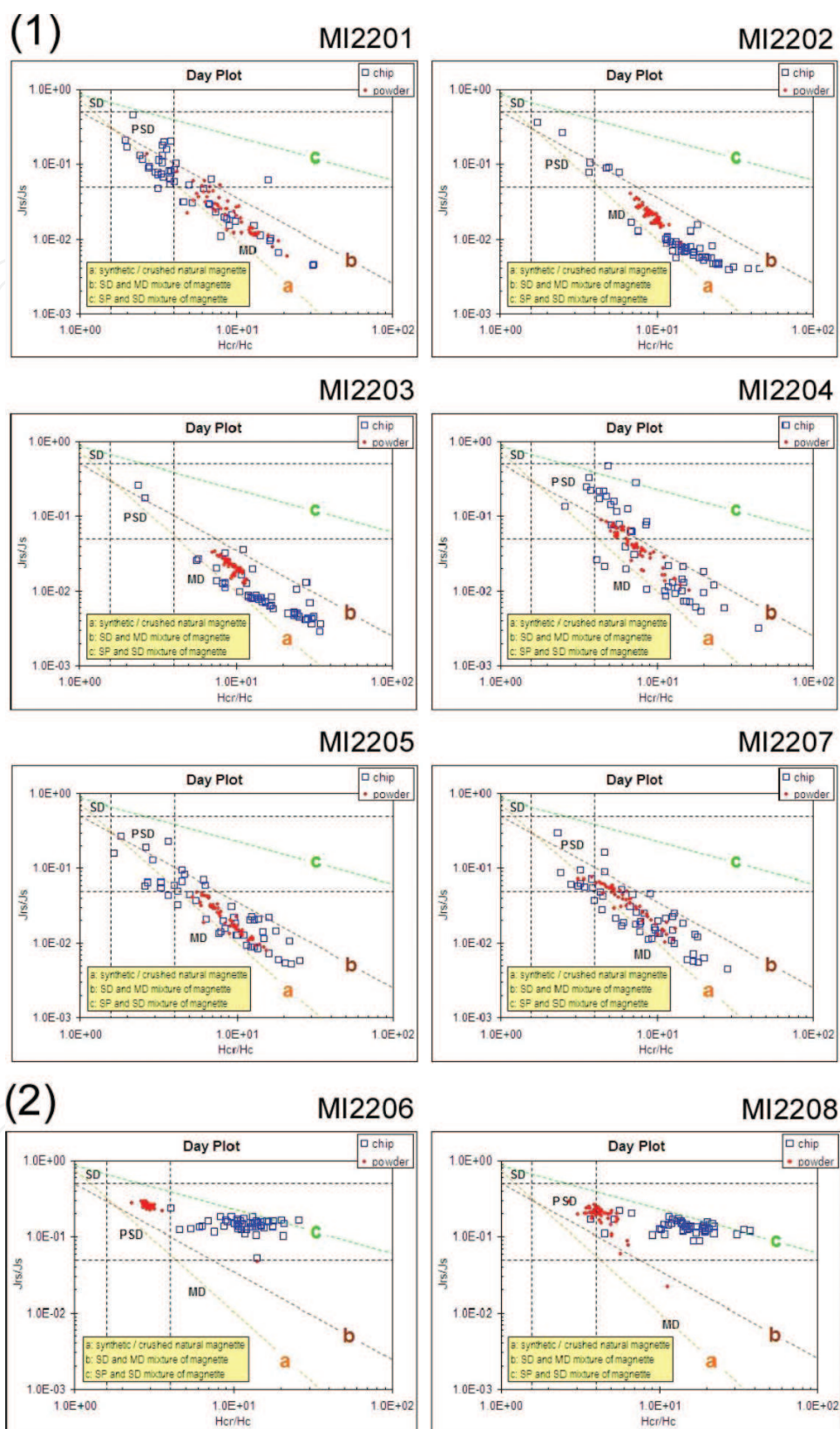


Figure 7. Logarithmic plots of hysteresis parameters [14] representing samples of fresh granite (1) and altered granite (2). See text for method of preparing chip and powder samples. Trends a, b and c originate from synthetic and crushed natural magnetite [15], single-domain (SD) and multidomain (MD) mixtures of magnetite [16] and superparamagnetic (SP) and SD mixtures of magnetite [17, 18], respectively.

Figure 8 shows examples of hysteresis loops for Toki Granite. The raw diagram seems to suggest an absence of ferromagnetic material. After correction to a linear gradient of paramagnetism, we are able to recognize a weak signature of ferromagnetic behavior. The wider loop of the altered granite (powder samples) is indicative of SD magnetite dominance. A noteworthy fact is that the altered chip sample exhibits the so-called wasp-waisted loop shape that originates from the presence of high-coercivity components related to a remagnetization event (e.g. [16]).

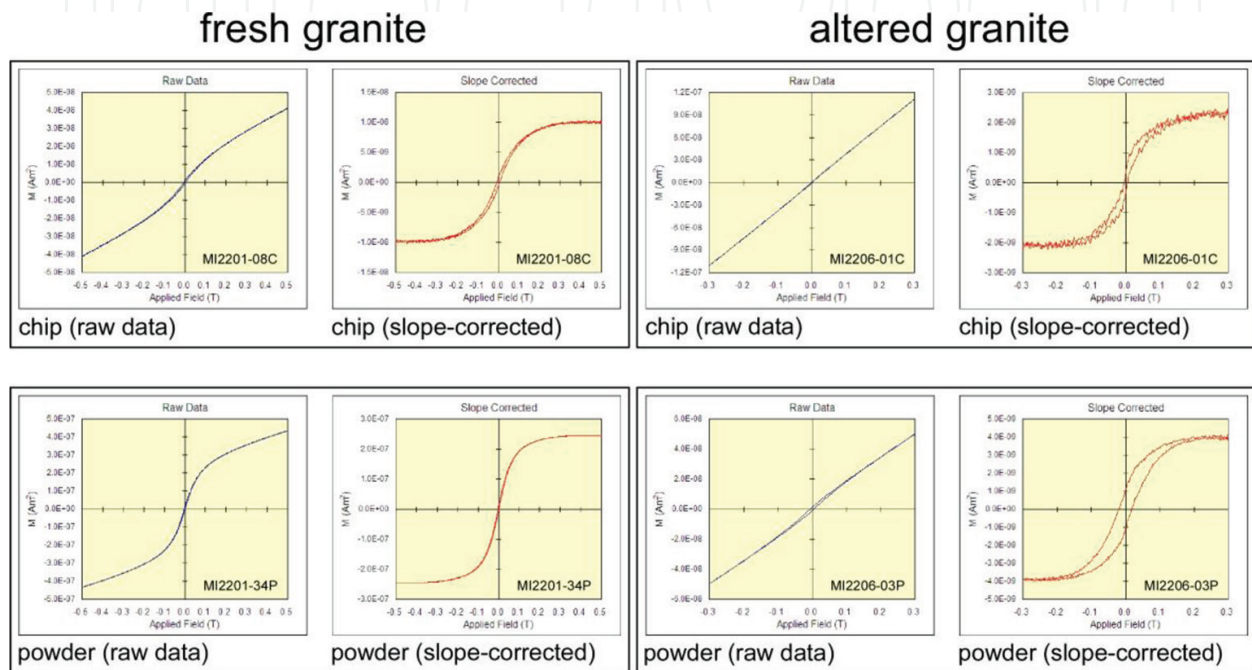


Figure 8. Examples of hysteresis loops for the Toki Granite (Blue: raw data, Red: data after correction to a linear gradient of paramagnetism). See text for preparation method of chip and powder samples.

Figure 9 shows logarithmic plots of bulk hysteresis parameters for 10 horizons of the Toki Granite measured on a vibrating sample magnetometer (VSM; MicroMag3900, Princeton Measurements Corporation) at the Center for Advanced Marine Core Research, Kochi University. Each sample, consisting of up to 1 cm³ of crushed rocks, was contained in a gelatin capsule for the measurements. This apparatus is able to deal with bulk samples including intrusives and reconfirmed the deviated trends of the altered granites and intrusive rocks.

3.4. Isothermal remanent magnetization (IRM) experiments

3.4.1. Spectrum of coercive force

In order to identify carriers of magnetic components in the samples, isothermal remanent magnetization (IRM) experiments were undertaken. Stepwise acquisition of IRM was performed according to an analytical technique developed by [19]. **Figure 10** shows a linear acquisition plot (LAP) and gradient of acquisition plot (GAP) of the IRM progressively acquired in direct

magnetic fields of up to about 3 T after pretreatment of alternating field demagnetization at 100 mT. The plots generated from a majority of the IRM data for fresh granite (a) can be matched by single magnetic components with relatively low $B_{1/2}$ values (18–25 mT; the field at which half of the IRM saturation is reached), indicating the existence of low coercive force (H_c) ferromagnetic mineral. On the basis of the T_{UB} spectra mentioned earlier, we consider that the remanent magnetization of the fresh granites resides in titanomagnetite.

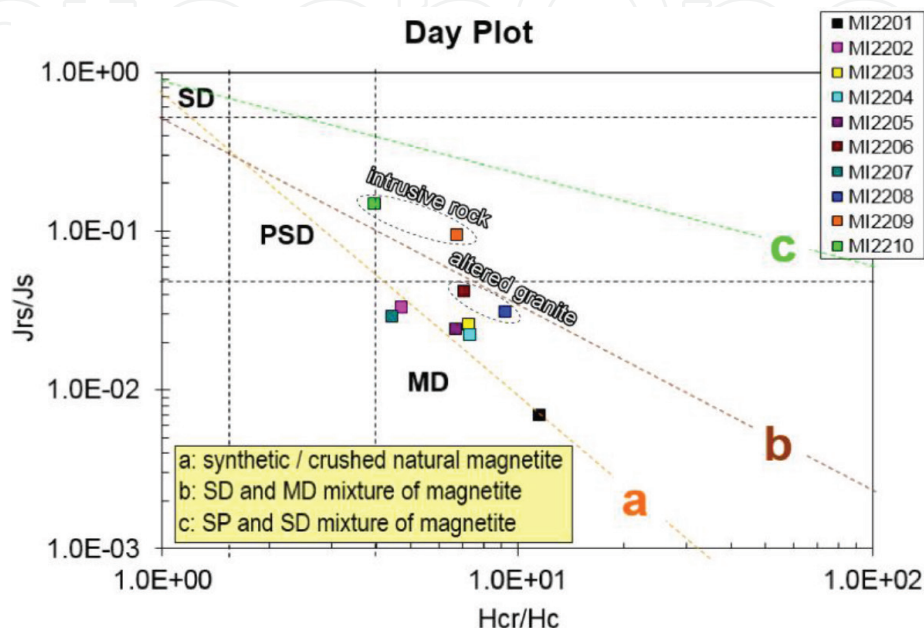


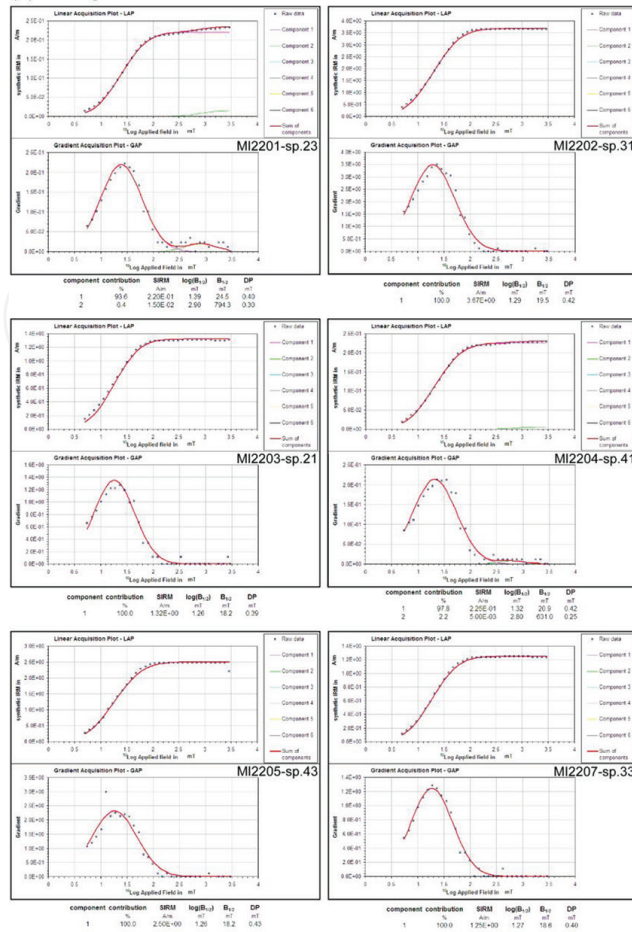
Figure 9. Logarithmic plots of bulk hysteresis parameters [14] for 10 horizons of the Toki Granite measured on a vibrating sample magnetometer (VSM). Trends a, b and c originate from synthetic and crushed natural magnetite [15], single-domain (SD) and multidomain (MD) mixtures of magnetite [16] and superparamagnetic (SP) and SD mixtures of magnetite [17, 18], respectively.

As for the altered granite (**Figure 10b**) and intrusive rock (c), the plots generated from the IRM data can be matched by two magnetic components with distinct $B_{1/2}$ values of 36–40 mT and 631–1122 mT, indicating the coexistence of low and high H_c ferromagnetic minerals. The contribution of the high H_c spectrum is overwhelming for intrusives. On the basis of the T_{UB} spectra mentioned before, we consider that the remanent magnetization of the samples that suffered a thermochemical change resides in titanomagnetite and hematite with various mixing ratios.

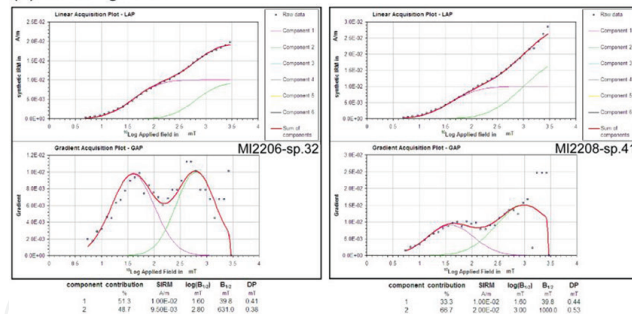
3.4.2. Thermal demagnetization of orthogonal IRMs

We executed PThD of composite IRMs for selected specimens. Based upon the procedure proposed by [20], composite IRMs were imparted by applying direct magnetic fields of 3.0, 0.4 and then 0.12 T onto the specimens in three orthogonal directions. As shown in **Figure 11**, the decay curve of the IRM components through PThD testing for fresh granite (a) indicates that the dominant magnetic phase is generally the low H_c (<0.12 T) soft fraction with a broad spectrum of T_{UB} up to 580°C. In such a case, the major carrier of the high- T_{UB} component of NRM is titanomagnetite.

(a) fresh granite



(b) altered granite



(c) intrusive rock

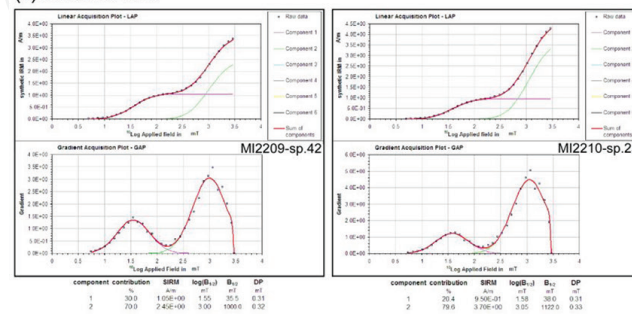


Figure 10. Linear acquisition plot (LAP) and gradient of acquisition plot (GAP) of isothermal remanent magnetization (IRM) acquired in direct magnetic fields of up to 3 T for fresh granite (a), altered granite (b) and intrusive rock (c). Specimens were processed after alternating field demagnetization at 100 mT.

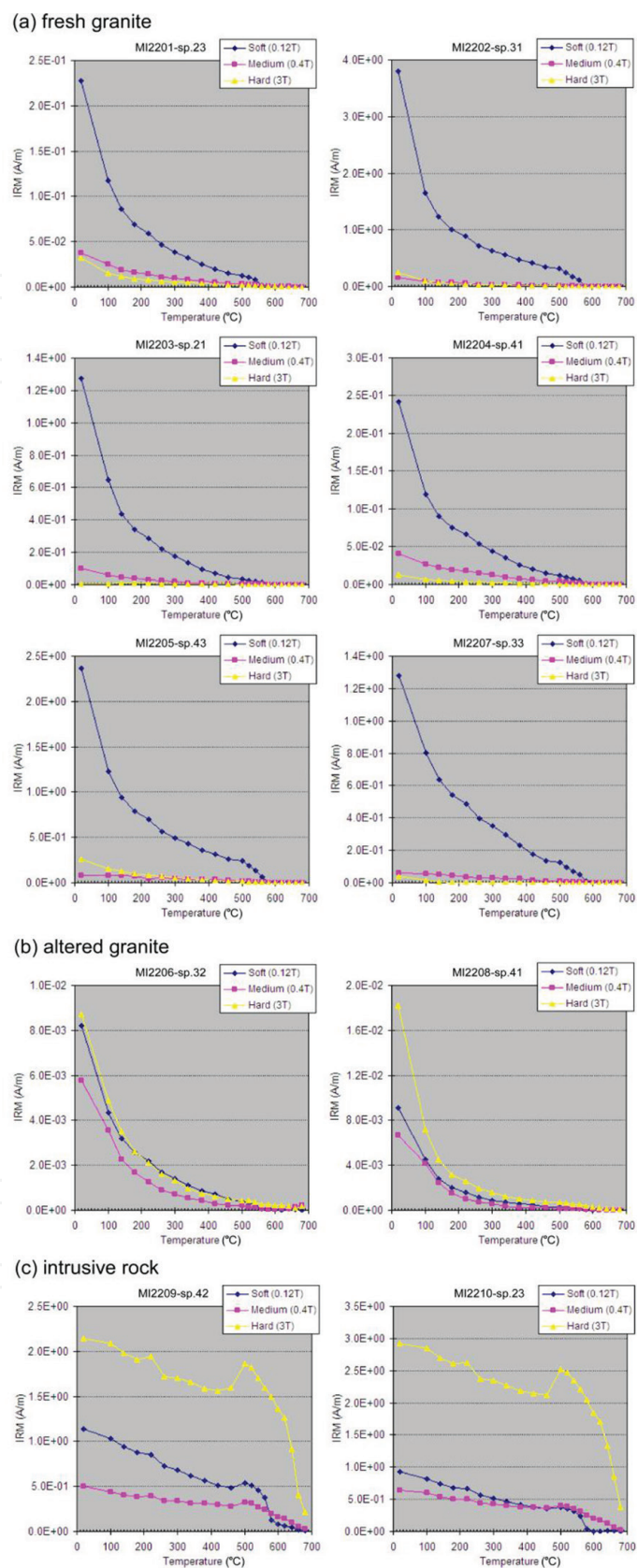


Figure 11. Thermal demagnetization curves of three orthogonal IRM components imparted on specimens from fresh granite (a), altered granite (b) and intrusive rock (c).

We identified both the medium ($0.12 < H_c < 0.4$ T) and hard ($0.4 < H_c < 3.0$ T) fractions for altered granite (b) and intrusive rock (c). In the altered granite, the medium ($T_{UB} < 580^\circ\text{C}$) and hard fractions ($T_{UB} < 680^\circ\text{C}$) are thought to be carried by SD-size magnetite and hematite, respectively. The medium ($T_{UB} < 680^\circ\text{C}$) and hard components ($T_{UB} < 680^\circ\text{C}$) of the intrusive rock probably reside in MD-size and SD-size hematite, respectively. Thus, the author has proven that the NRMs preserved in the underground samples are carried by mixture of titanomagnetite and hematite at various mixing ratios.

3.5. Magnetic susceptibility fabrics

Figure 12 presents the magnitudes of the magnetic fabrics in core samples with various lithologies. Obviously, thermochemical change results in remarkable decreases in the degree of anisotropy (P_j). It is also noteworthy that the shape parameter (T) values of the altered granites and intrusive rocks are in positive domain without exception, suggesting an oblate AMS fabric.

Figure 13 delineates the site-mean AMS fabrics of (a) fresh Toki Granite and (b) altered granite and intrusive rock. The fabric of the intact pluton has quite a large scatter, and no specific directional trend is observed. In sharp contrast with this, the principal AMS axes of the altered granites and intrusive rocks are tightly clustered with similar orientations. Considering the very weak ferromagnetic signature in the raw hysteresis loops (see Section 3.3), the fabric would appear to be carried by both authigenic iron oxides and platy grains of iron-bearing silicate minerals such as biotite or chlorite, whose shape anisotropy enhances the degree of AMS.

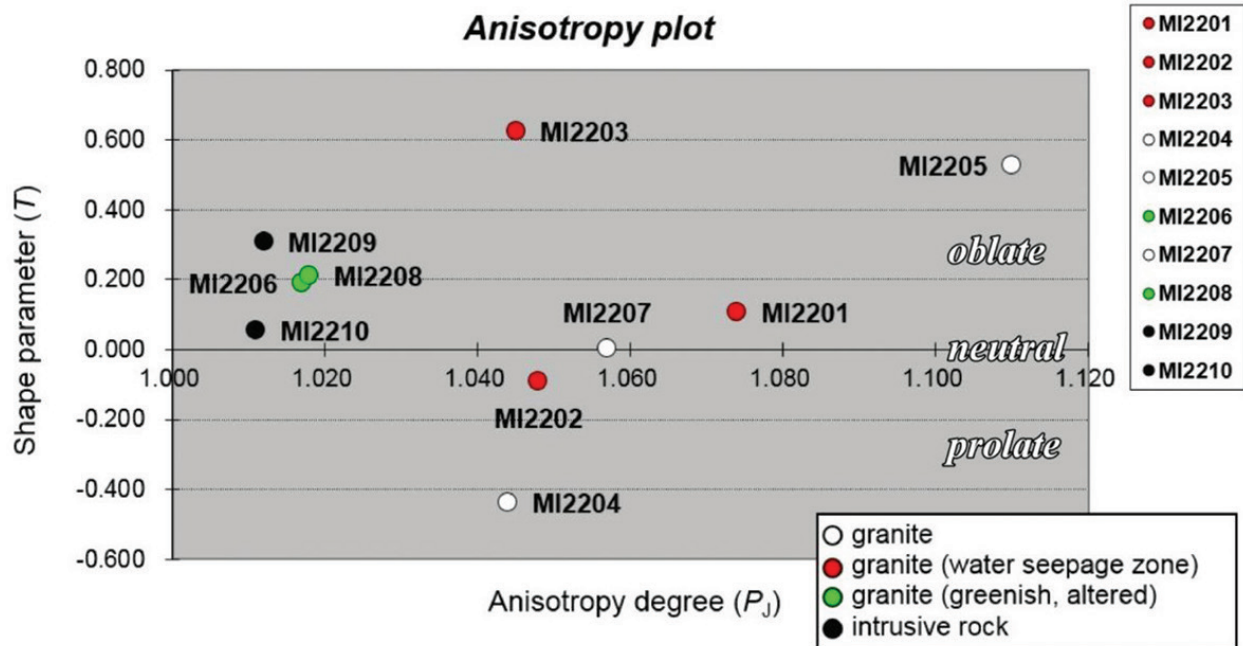


Figure 12. Magnitudes of magnetic fabrics in core samples with various lithologies.

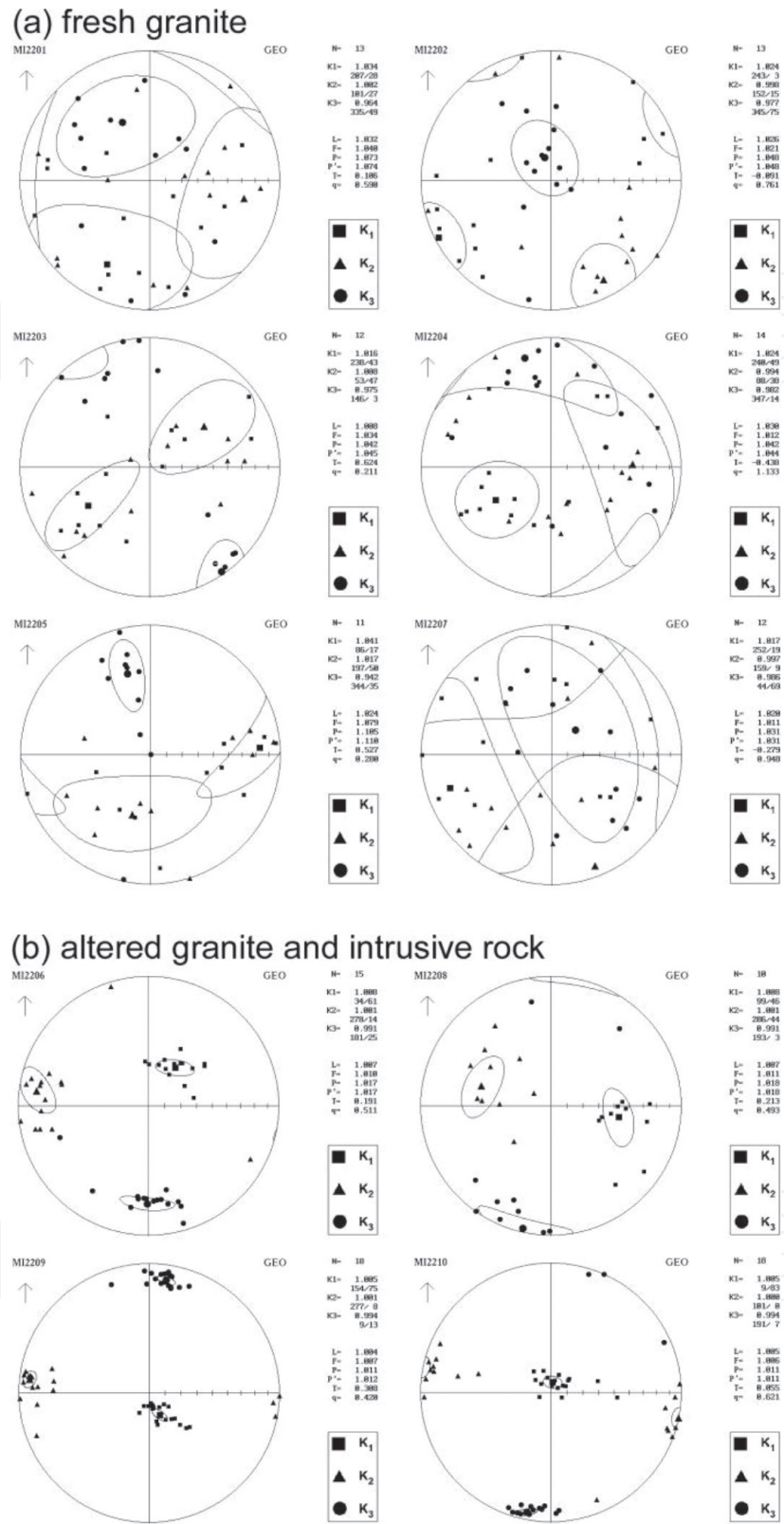


Figure 13. Anisotropy of magnetic susceptibility (AMS) fabric (principal susceptibility axes) for all specimens from the core sampling sites of the Toki Granite plotted on the lower hemisphere of equal-area projections. Data are shown in geographic coordinates. Ovals surrounding the mean directions of the three axes (shown by larger symbols) are 95% confidence regions. AMS data are presented in two groups, fresh granite (a) and altered granite and intrusive rock (b), which show similar fabrics.

4. Temporal transition of tectonic stress

Our rock magnetic experiments suggested a conspicuous AMS fabric in the altered granites and intrusive rocks. For intrusive rocks, magnetic anisotropy is generally related to an intrusion process, namely, the maximum and intermediate axes are bound to the flow plane of the magma [2]. On the assumption that the AMS-carrying ferromagnetic and paramagnetic minerals in the altered granites were precipitated and aligned on the surface of inherently orthogonal cooling fractures in the granites [4], the magnetic anisotropy can act as a proxy for the dike swarm that indicates paleostress field. As the authigenic minerals tend to grow on the most permeable open fracture network, the foliation plane of the anisotropy ellipsoid, which is perpendicular to the minimum axis (K_3), is expected to be parallel to dike elongation. In the next section, the author reviews previous studies of tectonic stress around the MIU site and tests the usability of the AMS data as a stress indicator.

4.1. Previous studies

Figure 14a presents orientation contour diagrams of healed microcracks (HCs), sealed microcracks (SCs) and open microcracks (OCs) in the Toki Granite for surface outcrops (upper) and the DH-15 borehole (lower) after [21]. They considered that the north-south trending HC data reflect the regional paleostress field, and assumed that they were formed around 60 Ma based on K-Ar ages of the pluton and the formation temperature (ca. 300–400°C) of fluid inclusions estimated from microthermometry for intrusion depth (3.5 km = 100 MPa). Later high-angle fracture sets of the SCs and OCs show quite a different trend and imply a remarkable change in the stress regime. The youngest OC was thought to be formed in the Miocene based on the exhumation and burial history of the granite, whereas the origin of the SCs filled with carbonate minerals was not clearly discussed.

In igneous terranes, paleostress study is often based on the azimuth of a dike swarm, which coincides with the $\sigma_{H_{\max}}$ direction at the time of intrusion [23]. Near the MIU site, there are two conspicuous sets of dikes within the Toki Granite. Hoshi and Nishimura [22] described the granitic body as having been first intruded by north-south trending aplite dikes and then cut by a high-magnesium andesite dike swarm with an east-west trend. As shown in **Figure 14b**, the three-dimensional orientations of the aplite and andesite dikes show a striking resemblance to those of the HC and SC/OC data of [21]. Their cross-cutting relationship is obvious in **Figure 14c**. Oikawa et al. [24] reported a K-Ar age of the high-magnesium andesite at 59.6 ± 1.4 Ma. This points to a drastic change in regional stress that may have been caused by a tectonic event around the end of the Cretaceous.

4.2. Radiometric dating

To consider the time sequence of stress changes envisaged from dike orientations, placing the timing of the aplite intrusion between the emplacement of the granitic pluton and the anomalous

activity of the high-magnesium andesite is of great importance. Therefore, the author executed radiometric dating on the igneous rock of unknown age.

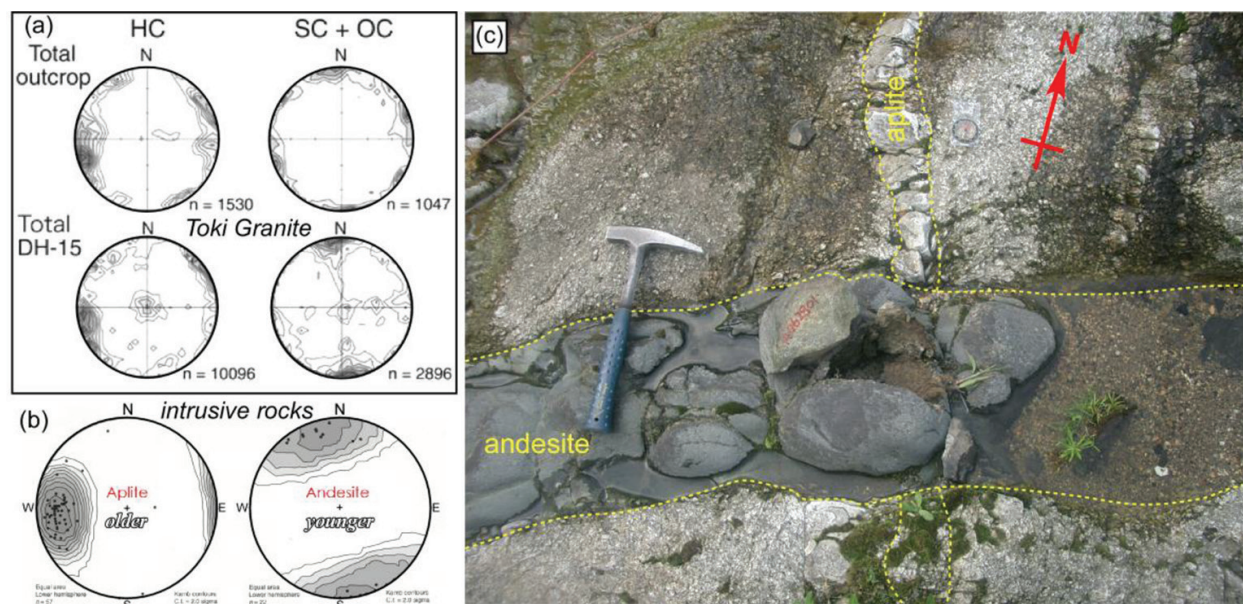


Figure 14. (a) Orientation contour diagrams of healed microcracks (HCs), sealed microcracks (SCs) and open microcracks (OCs) in the Toki Granite for surface outcrops (upper) and the DH-15 borehole (lower) after [21]. (b) Poles of aplite dikes (left) and andesite dikes (right) intruded in the Toki Granite after [22]. (c) Photo of an outcrop showing cross-cutting relationship between intrusive rocks hosted by the Toki Granite.

4.2.1. Samples

Dating samples were taken from an outcrop (Lat. = 35.3522°N, Long. = 137.1715°E) by the Toki River running through exposures of the Cretaceous granites. Samples 14062801 and 14062802 were obtained from the andesitic dike and the aplite, respectively. Leucocratic aplite (Sp. 14062802) yielded affluent zircon grains during mineral separation, whereas the andesite lacked them. Hence, we concentrated on the aplite sample.

4.2.2. Methods

The fission track (FT) dating method is after [25]. U-Pb age data were obtained using inductively coupled plasma-mass spectrometry (ICP-MS) combined with an excimer laser ablation (LA) sample introduction system. The U-Pb age determinations on zircon samples were performed after chemical leaching using 47% HF for 20 hours at room temperature or after FT etching using a KOH-NaOH eutectic solution for 22 hours at 225°C.

4.2.3. Results

The results of the FT dating of the zircon grains are summarized in **Table 1a** and **Figure 15a**. Analysis was executed on a total of 15 crystals and provided a weighted mean age of 53.2 ± 2.6

Ma. The results of a chi-squared test were negative because of considerable variation of uranium concentration as anticipated from the samples' strong zonal arrangement.

No.	Ns	Nu	$S \times 10^{-5} \text{ (cm}^2\text{)}$	$\rho_s \times 10^{-7} \text{ (cm}^{-2}\text{)}$	$\rho_u \times 10^{-9} \text{ (cm}^{-2}\text{)}$	$Ns/Nu \times 10^3$	T (Ma)	σ_T (Ma)	U (ppm)
14	26	457	0.20	1.30	2.29	56.89	99.48	20.36	250
11	83	1631	1.00	0.83	1.63	50.89	89.06	10.50	178
15	16	317	0.40	0.40	0.79	50.47	88.33	22.85	87
2	73	1461	1.20	0.61	1.22	49.97	87.45	10.93	133
7	36	751	0.60	0.60	1.25	47.94	83.92	14.62	137
4	55	1227	0.80	0.69	1.53	44.82	78.51	11.17	168
9	99	2656	1.20	0.83	2.21	37.27	65.35	7.07	242
12	86	2401	1.00	0.86	2.40	35.82	62.81	7.24	262
6	79	2848	1.00	0.79	2.85	27.74	48.70	5.81	311
13	59	2266	0.60	0.98	3.78	26.04	45.72	6.24	413
1	62	2524	0.60	1.03	4.21	24.56	43.14	5.75	460
3	31	1484	0.60	0.52	2.47	20.89	36.71	6.79	270
8	29	1420	1.20	0.24	1.18	20.42	35.89	6.85	129
10	56	2840	1.20	0.47	2.37	19.72	34.65	4.83	259
5	61	3771	0.90	0.68	4.19	16.18	28.44	3.81	458

Ns is number of spontaneous tracks, Nu is number of ^{238}U counts, S is analyzed area of crystal, ρ_s is density of spontaneous tracks, ρ_u is density of ^{238}U counts, σ_T is error for each grain age (1σ), U is uranium density. Uranium concentration for standardization using 91,500 standard zircon is $0.864 \times 10^6 \text{ cm}^2$. Epsilon (ϵ) corresponding to conventional zeta (ζ) value for Fish Canyon Tuff zircon is 40.8 ± 1.4 .

Table 1a. Fission-track grain ages of zircons obtained from Sp. 14062802.

Figure 15b compares FT and U-Pb ages for zircons obtained from the aplite. The closing temperature for U-Pb ages is about 900°C in a laboratory or $>700^\circ\text{C}$ in natural conditions, whereas that for zircon FT ages is $240 \sim 250^\circ\text{C}$ for heating over a period of 1 million years. Reflecting the difference, the U-Pb ages tend to be older with smaller scatter than the FT ages.

Results of the U-Pb dating for the zircon grains are summarized in **Table 1b** (all analyzed grains) and **Table 1c** (adopted grains). Based on the concordia plot for U-Pb zircon ages in **Figure 15c**, we excluded zircon grains with discordant data then adopted concordant grains to calculate the average. The final result is presented in **Figure 15d**.

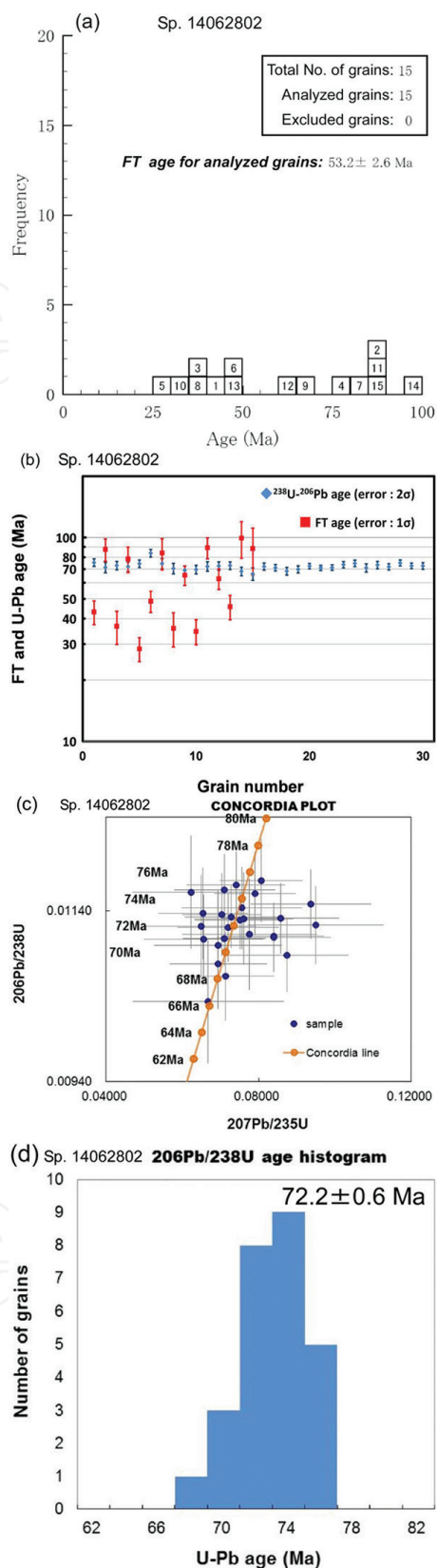


Figure 15. Radiometric dating of an aplite dike intruded in the Toki Granite (Sp. 14062802; Lat. = 35.3522°N, Long. = 137.1715°E). (a) Results of fission-track (FT) dating of zircons. (b) FT and U-Pb age plots for zircons. (c) Concordia plot for U-Pb ages of zircons. (d) Result of U-Pb dating of zircons.

Sample name	Total count						Isotopic ratios						Disc.*	Age (Ma)				
	²⁰⁶ Pb	²⁰⁷ Pb	²³² Th	²³⁵ U	²³⁸ U	Th	²⁰⁷ Pb	Error 2σ	²⁰⁶ Pb	Error 2σ	²⁰⁷ Pb	Error 2σ		²⁰⁶ Pb	Error	²⁰⁷ Pb	Error	
						U	²⁰⁶ Pb		²³⁸ U		²³⁵ U		²³⁸ U	2σ	²³⁵ U	2σ		
14062802	no.1	6472	327	698999	5389	742999	1.10	0.0505	±0.0045	0.01176	±0.000491	0.0808	±0.0109	concordant	75.4	±3.2	78.9	±11.0
14062802	no.2	1772	91	99999	1559	214999	0.55	0.0514	±0.0046	0.01113	±0.000649	0.0777	±0.0176	concordant	71.3	±4.2	75.9	±17.8
14062802	no.3	3682	156	158999	3169	436999	0.43	0.0424	±0.0038	0.01138	±0.000536	0.0655	±0.0117	concordant	72.9	±3.5	64.4	±11.8
14062802	no.4	2252	96	136999	1965	270999	0.59	0.0426	±0.0038	0.01122	±0.000606	0.0650	±0.0144	concordant	71.9	±3.9	63.9	±14.5
14062802	no.5	6362	319	314999	5367	739999	0.50	0.0501	±0.0045	0.01161	±0.000486	0.0791	±0.0107	concordant	74.4	±3.1	77.3	±10.8
14062802	no.6	4872	356	403999	3648	502999	0.94	0.0731	±0.0065	0.01308	±0.000578	0.1299	±0.0171	-23	83.8	±3.7	124.0	±17.3
14062802	no.7	1902	75	112999	1603	220999	0.60	0.0394	±0.0035	0.01162	±0.000662	0.0623	±0.0154	concordant	74.5	±4.3	61.3	±15.5
14062802	no.8	1702	79	138999	1516	208999	0.78	0.0464	±0.0041	0.01100	±0.000650	0.0694	±0.0168	concordant	70.5	±4.2	68.1	±16.9
14062802	no.9	3122	148	379999	2836	390999	1.14	0.0474	±0.0042	0.01078	±0.000530	0.0695	±0.0127	concordant	69.1	±3.4	68.2	±12.8
14062802	no.10	3362	238	359999	3032	417999	1.01	0.0708	±0.0063	0.01086	±0.000523	0.1045	±0.0159	-17	69.6	±3.4	100.9	±16.0
14062802	no.11	2402	77	168999	2089	287999	0.69	0.0321	±0.0028	0.01126	±0.000596	0.0491	±0.0119	16	72.2	±3.8	48.6	±12.0
14062802	no.12	3552	176	150999	3075	423999	0.42	0.0495	±0.0044	0.01131	±0.000537	0.0762	±0.0130	concordant	72.5	±3.5	74.5	±13.1
14062802	no.13	5612	256	362999	4838	666999	0.64	0.0456	±0.0041	0.01136	±0.000487	0.0704	±0.0103	concordant	72.8	±3.1	69.1	±10.4
14062802	no.14	3182	157	103999	2930	403999	0.30	0.0493	±0.0044	0.01063	±0.000520	0.0713	±0.0127	concordant	68.2	±3.3	69.9	±12.9
14062802	no.15	1072	51	90999	1015	139999	0.76	0.0476	±0.0042	0.01034	±0.000722	0.0668	±0.0198	concordant	66.3	±4.7	65.7	±19.9
14062802	no.16	3036	188	157998	2654	365999	0.51	0.0619	±0.0068	0.01124	±0.000456	0.0950	±0.0178	concordant	72.0	±2.9	92.1	±17.9
14062802	no.17	3946	219	166998	3496	481999	0.41	0.0555	±0.0061	0.01109	±0.000406	0.0840	±0.0149	concordant	71.1	±2.6	81.9	±15.1
14062802	no.18	2606	166	147998	2401	330999	0.52	0.0637	±0.0070	0.01067	±0.000461	0.0927	±0.0181	-1	68.4	±3.0	90.0	±18.2
14062802	no.19	3246	191	150998	2930	403999	0.44	0.0588	±0.0065	0.01089	±0.000430	0.0874	±0.0162	concordant	69.8	±2.8	85.1	±16.4
14062802	no.20	7076	345	700998	6158	848999	0.97	0.0488	±0.0054	0.01129	±0.000337	0.0751	±0.0117	concordant	72.4	±2.2	73.6	±11.9
14062802	no.21	8256	388	389998	7325	1009999	0.45	0.0470	±0.0052	0.01107	±0.000315	0.0710	±0.0108	concordant	71.0	±2.0	69.7	±10.9
14062802	no.22	6436	357	734998	5693	784999	1.10	0.0555	±0.0061	0.01111	±0.000342	0.0841	±0.0131	concordant	71.2	±2.2	82.0	±13.2

Sample name	Total count					Isotopic ratios								Disc.*	Age (Ma)			
	²⁰⁶ Pb	²⁰⁷ Pb	²³² Th	²³⁵ U	²³⁸ U	Th U	²⁰⁷ Pb ²⁰⁶ Pb	Error 2σ	²⁰⁶ Pb ²³⁸ U	Error 2σ	²⁰⁷ Pb ²³⁵ U	Error 2σ	²⁰⁶ Pb ²³⁸ U		Error 2σ	²⁰⁷ Pb ²³⁵ U	Error 2σ	
14062802 no.23	4416	264	443998	3779	520999	1.00	0.0598	±0.0066	0.01148	±0.000403	0.0937	±0.0158	concordant	73.6	±2.6	90.9	±15.9	
14062802 no.24	4136	185	172998	3489	480999	0.42	0.0447	±0.0049	0.01165	±0.000419	0.0711	±0.0133	concordant	74.7	±2.7	69.7	±13.4	
14062802 no.25	2166	94	126998	1922	264999	0.56	0.0434	±0.0048	0.01107	±0.000517	0.0656	±0.0156	concordant	71.0	±3.3	64.5	±15.8	
14062802 no.26	2786	135	148998	2393	329999	0.53	0.0485	±0.0053	0.01144	±0.000481	0.0756	±0.0158	concordant	73.3	±3.1	74.0	±15.9	
14062802 no.27	4096	193	294998	3590	494999	0.70	0.0471	±0.0052	0.01121	±0.000405	0.0721	±0.0133	concordant	71.9	±2.6	70.7	±13.4	
14062802 no.28	5046	234	264998	4236	583999	0.53	0.0464	±0.0051	0.01171	±0.000392	0.0741	±0.0129	concordant	75.0	±2.5	72.6	±13.0	
14062802 no.29	5646	266	328998	4896	674999	0.57	0.0471	±0.0052	0.01133	±0.000364	0.0729	±0.0122	concordant	72.6	±2.3	71.4	±12.3	
14062802 no.30	3976	221	217998	3452	475999	0.54	0.0556	±0.0061	0.01132	±0.000413	0.0858	±0.0152	concordant	72.5	±2.7	83.6	±15.3	
Average ± 2SD														72.2	±6.1	76.1	±28.0	
Weighted average														72.2	±0.5	74.3	±2.5	

Th/U is ratio of thorium and uranium concentrations. Disc.* is degree of discordance. Positive and negative values mean left- and right-side significant offsets from concordia line, respectively.

Table 1b. U-Pb ages for all analyzed zircon grains obtained from Sp. 14062802.

Sample name	Total count						Isotope ratios						Disc.*	Age (Ma)				
	²⁰⁶ Pb	²⁰⁷ Pb	²³² Th	²³⁵ U	²³⁸ U	Th	²⁰⁷ Pb	Error	²⁰⁶ Pb	Error	²⁰⁷ Pb	Error		²⁰⁶ Pb	Error	²⁰⁷ Pb	Error	
						U	²⁰⁶ Pb	2σ	²³⁸ U	2σ	²³⁵ U	2σ		²³⁸ U	2σ	²³⁵ U	2σ	
14062802	no.1	6472	327	698999	5389	742999	1.10	0.0505	±0.0045	0.01176	±0.000491	0.0808	±0.0109	concordant	75.4	±3.2	78.9	±11.0
14062802	no.2	1772	91	99999	1559	214999	0.55	0.0514	±0.0046	0.01113	±0.000649	0.0777	±0.0176	concordant	71.3	±4.2	75.9	±17.8
14062802	no.3	3682	156	158999	3169	436999	0.43	0.0424	±0.0038	0.01138	±0.000536	0.0655	±0.0117	concordant	72.9	±3.5	64.4	±11.8
14062802	no.4	2252	96	136999	1965	270999	0.59	0.0426	±0.0038	0.01122	±0.000606	0.0650	±0.0144	concordant	71.9	±3.9	63.9	±14.5
14062802	no.5	6362	319	314999	5367	739999	0.50	0.0501	±0.0045	0.01161	±0.000486	0.0791	±0.0107	concordant	74.4	±3.1	77.3	±10.8
14062802	no.7	1902	75	112999	1603	220999	0.60	0.0394	±0.0035	0.01162	±0.000662	0.0623	±0.0154	concordant	74.5	±4.3	61.3	±15.5
14062802	no.8	1702	79	138999	1516	208999	0.78	0.0464	±0.0041	0.01100	±0.000650	0.0694	±0.0168	concordant	70.5	±4.2	68.1	±16.9
14062802	no.9	3122	148	379999	2836	390999	1.14	0.0474	±0.0042	0.01078	±0.000530	0.0695	±0.0127	concordant	69.1	±3.4	68.2	±12.8
14062802	no.12	3552	176	150999	3075	423999	0.42	0.0495	±0.0044	0.01131	±0.000537	0.0762	±0.0130	concordant	72.5	±3.5	74.5	±13.1
14062802	no.13	5612	256	362999	4838	666999	0.64	0.0456	±0.0041	0.01136	±0.000487	0.0704	±0.0103	concordant	72.8	±3.1	69.1	±10.4
14062802	no.14	3182	157	103999	2930	403999	0.30	0.0493	±0.0044	0.01063	±0.000520	0.0713	±0.0127	concordant	68.2	±3.3	69.9	±12.9
14062802	no.15	1072	51	90999	1015	139999	0.76	0.0476	±0.0042	0.01034	±0.000722	0.0668	±0.0198	concordant	66.3	±4.7	65.7	±19.9
14062802	no.16	3036	188	157998	2654	365999	0.51	0.0619	±0.0068	0.01124	±0.000456	0.0950	±0.0178	concordant	72.0	±2.9	92.1	±17.9
14062802	no.17	3946	219	166998	3496	481999	0.41	0.0555	±0.0061	0.01109	±0.000406	0.0840	±0.0149	concordant	71.1	±2.6	81.9	±15.1
14062802	no.19	3246	191	150998	2930	403999	0.44	0.0588	±0.0065	0.01089	±0.000430	0.0874	±0.0162	concordant	69.8	±2.8	85.1	±16.4
14062802	no.20	7076	345	700998	6158	848999	0.97	0.0488	±0.0054	0.01129	±0.000337	0.0751	±0.0117	concordant	72.4	±2.2	73.6	±11.9
14062802	no.21	8256	388	389998	7325	1009999	0.45	0.0470	±0.0052	0.01107	±0.000315	0.0710	±0.0108	concordant	71.0	±2.0	69.7	±10.9
14062802	no.22	6436	357	734998	5693	784999	1.10	0.0555	±0.0061	0.01111	±0.000342	0.0841	±0.0131	concordant	71.2	±2.2	82.0	±13.2
14062802	no.23	4416	264	443998	3779	520999	1.00	0.0598	±0.0066	0.01148	±0.000403	0.0937	±0.0158	concordant	73.6	±2.6	90.9	±15.9
14062802	no.24	4136	185	172998	3489	480999	0.42	0.0447	±0.0049	0.01165	±0.000419	0.0711	±0.0133	concordant	74.7	±2.7	69.7	±13.4
14062802	no.25	2166	94	126998	1922	264999	0.56	0.0434	±0.0048	0.01107	±0.000517	0.0656	±0.0156	concordant	71.0	±3.3	64.5	±15.8
14062802	no.26	2786	135	148998	2393	329999	0.53	0.0485	±0.0053	0.01144	±0.000481	0.0756	±0.0158	concordant	73.3	±3.1	74.0	±15.9

Sample name	Total count						Isotope ratios						Disc.*	Age (Ma)			
	²⁰⁶ Pb	²⁰⁷ Pb	²³² Th	²³⁵ U	²³⁸ U	Th	²⁰⁷ Pb	Error	²⁰⁶ Pb	Error	²⁰⁷ Pb	Error		²⁰⁶ Pb	Error	²⁰⁷ Pb	Error
						U	²⁰⁶ Pb	2σ	²³⁸ U	2σ	²³⁵ U	2σ		²³⁸ U	2σ	²³⁵ U	2σ
14062802 no.27	4096	193	294998	3590	494999	0.70	0.0471	±0.0052	0.01121	±0.000405	0.0721	±0.0133	concordant	71.9	±2.6	70.7	±13.4
14062802 no.28	5046	234	264998	4236	583999	0.53	0.0464	±0.0051	0.01171	±0.000392	0.0741	±0.0129	concordant	75.0	±2.5	72.6	±13.0
14062802 no.29	5646	266	328998	4896	674999	0.57	0.0471	±0.0052	0.01133	±0.000364	0.0729	±0.0122	concordant	72.6	±2.3	71.4	±12.3
14062802 no.30	3976	221	217998	3452	475999	0.54	0.0556	±0.0061	0.01132	±0.000413	0.0858	±0.0152	concordant	72.5	±2.7	83.6	±15.3
Average ± 2SD														72.0	±4.2	73.8	±16.4
Weighted average														72.2	±0.6	73.3	±2.7

Th/U is ratio of thorium and uranium concentrations. Disc.* is degree of discordance. Positive and negative values mean left- and right-side significant offsets from concordia line, respectively.

Table 1c. U-Pb ages for adopted zircon grains obtained from Sp. 14062802.

5. Discussion

5.1. Time sequence of igneous activity

A chronological study by the author obtained a U-Pb age of 72.2 ± 0.6 Ma for the aplite dike intruded into the Toki Granite. Considering the ages reported for the host rock [7–9], the dike swarm was emplaced in the final stage of the Late Cretaceous extensive igneous activity, as Kinoshita [26] interpreted as resulting from subduction of oceanic plates' divergent margin. Oikawa et al. [24] stated that their K-Ar age for the andesitic dike provides the upper limit of the intrusion event. They also pointed out two stages of formation of high-magnesium andesite, which is suggestive of thermal input around the continental margin. Such a thermal event may be related to ridge subduction as conceived by [26] or, alternatively, with an asthenospheric injection that provoked crustal thinning and deformation of the Far East [27].

5.2. Tectonic context of stress regimes

The azimuth of the aplite dike swarm is indicative of a north-south $\sigma_{H_{max}}$ direction at around the end of the Cretaceous, whereas those of the andesite dike swarm and our AMS fabric acquired during a thermochemical event in the early Paleogene imply a drastic change of $\sigma_{H_{max}}$ trend into an east-west direction. We assume that the regional stress is reflected in a wrench deformation mode of the continental margin, which was controlled by lateral motions on the longstanding Median Tectonic Line as advocated by [28]. **Figure 16** presents the Late Cretaceous to Paleocene tectonic stress transition around the eastern part of southwest Japan inferred from geologic evidences. As clarified by [29], the deformation process of the forearc accretionary complex of southwest Japan implies an enigmatic shift of shearing modes: sinistral to dextral after 89 Ma and dextral to sinistral before 76 Ma. The present study seems to indicate that the older stress regime's unraveling (**Figure 16** left) is related to the sinistral stage since ca. 76 Ma based on the timing of felsic magma activity and the aplite intrusion. The tectonic context of the younger regime, confirmed by the azimuth of the anomalous andesite dike swarm and the AMS fabric of the Toki pluton, will be understood through further effort to determine the regional extent and duration of the stress state.

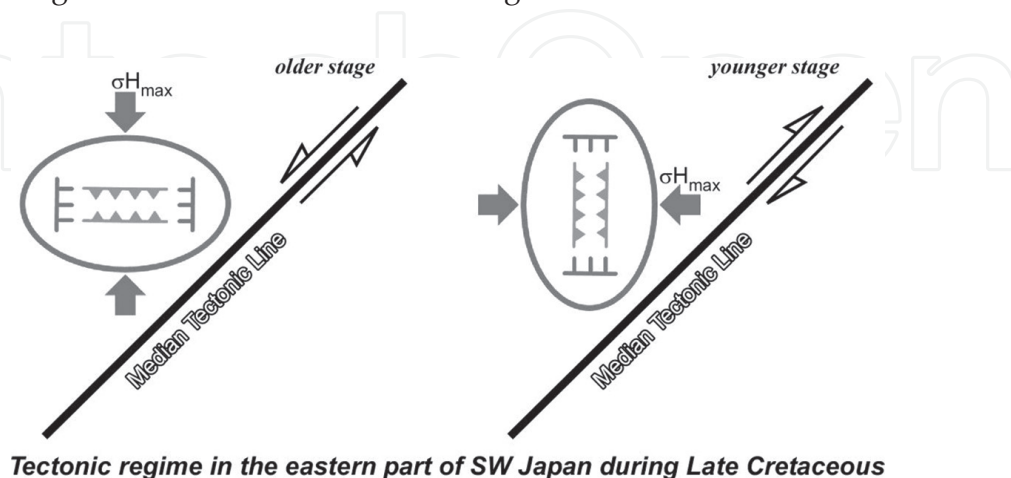


Figure 16. Late Cretaceous to Paleocene tectonic stress transition around the eastern part of southwest Japan inferred from geologic evidences presented in **Figure 14**.

6. Conclusions

Well-organized rock magnetic and geochronological investigations have revealed the origin of a unique magnetic fabric of a granitic pluton in the eastern part of southwest Japan. The Late Cretaceous Toki Granite suffered a thermochemical event, which resulted in tightly grouped principal axes of the anisotropy of magnetic susceptibility (AMS). The magnetic fabrics originate from ferromagnetic and paramagnetic minerals precipitated on fracture surfaces developed under regional tectonic stress. Together with previous studies of microcrack generation and dike intrusion in the Toki Granite, the AMS fabric delineates a drastic shift in tectonic stress state along the Asian continental margin from the Late Cretaceous to the early Paleogene.

Acknowledgements

The author is grateful to Eiji Sasao, Takashi Yuguchi and Masayuki Ishibashi for their earnest support and advice during the course of sampling at the Mizunami Underground Research Laboratory of the Japan Atomic Energy Agency and the succeeding data analysis. The author also extends his hearty appreciation to Naoto Ishikawa and Yuhji Yamamoto for the use of the rock magnetic laboratories at Kyoto University and the Center for Advanced Marine Core Research of Kochi University, respectively. Thanks are also due to Takashi Inoue for his efforts during the experiments.

Author details

Yasuto Itoh

Address all correspondence to: yasutokov@yahoo.co.jp

Graduate School of Science, Osaka Prefecture University, Osaka, Japan

References

- [1] Hrouda F, Lanza R. Magnetic fabric in the Biella and Traversella stocks (Periadriatic Line): implications for the emplacement mode. *Physics of the Earth and Planetary Interiors*. 1989; 56: 337–348.
- [2] Tarling DH, Hrouda F. *The Magnetic Anisotropy of Rocks*. London: Chapman & Hall; 1993. 217 p.
- [3] Itoh Y, Amano K. Progressive segmentation and systematic block rotation within a plutonic body: palaeomagnetism of the Cretaceous Kurihashi granodiorite in northeast Japan. *Geophysical Journal International*. 2004; 157: 128–140.

- [4] Vollbrecht A, Rust S, Weber K. Development of microcracks in granites during cooling and uplift: examples from the Variscan basement in NE Bavaria, Germany. *Journal of Structural Geology*. 1991; 13: 787–799.
- [5] Geological Survey of Japan, AIST, editor. Seamless Digital Geological Map of Japan 1:200,000 (July 3, 2012 Version), Research Information Database DB084. Tsukuba: Geological Survey of Japan, AIST (National Institute of Advanced Industrial Science and Technology); 2012.
- [6] Yamashita N, Kaseno Y, Itoigawa J, editors. *Regional Geology of Japan – Part 5 Chubu II*. Tokyo: Kyoritsu Shuppan Co.; 1988. 310 p.
- [7] Suzuki K, Adachi M. Denudation history of the high T/P Ryoke metamorphic belt, southwest Japan: constraints from CHIME monazite ages of gneisses and granitoids. *Journal of Metamorphic Geology*. 1998; 16: 23–37.
- [8] Shibata K, Ishihara S. Rb-Sr whole-rock and K-Ar mineral ages of granitic rocks in Japan. *Geochemical Journal*. 1979; 13: 113–119.
- [9] Yuguchi T, Tsuruta T, Hama K, Nishiyama T. The spatial variation of initial $^{87}\text{Sr}/^{86}\text{Sr}$ ratios in the Toki granite, central Japan: implications for the intrusion and cooling processes of a granitic pluton. *Journal of Mineralogical and Petrological Sciences*. 2013; 108: 1–12.
- [10] Ishihara S, Suzuki Y. Basement granites of the Toki uranium deposits in Tono region. *Reports of the Geological Survey of Japan*. 1969; 232: 113–127.
- [11] Kirschvink JL. The least-squares line and plane and the analysis of palaeomagnetic data. *Geophysical Journal of the Royal Astronomical Society*. 1980; 62: 699–718.
- [12] Sasao E, Yuguchi T, Itoh Y, Inoue T, Ishibashi M. Formative mechanism of inhomogeneous distribution of fractures, an example of the Toki Granite, Central Japan. In: *Proceedings of 10th Asian Regional Conference of IAEG*; 26–29 Sept. 2015; Uji. 6 p. (http://2015ars.com/arc/data/TP3/TP3-P01_1075939_1493692.pdf)
- [13] Heller F, Liu XM, Liu TS, Xu TC. Magnetic susceptibility of loess in China. *Earth and Planetary Science Letters*. 1991; 103: 301–310.
- [14] Day R, Fuller M, Schmidt VA. Hysteresis properties of titanomagnetites: grain-size and compositional dependence. *Physics of the Earth and Planetary Interiors*. 1977; 13: 260–267.
- [15] Dunlop DJ. Hysteresis properties of magnetite and their dependence on particle size: a test of pseudo-single-domain remanence models. *Journal of Geophysical Research*. 1986; 91: 9569–9584.
- [16] Channell JET, McCabe C. Comparison of magnetic hysteresis parameters of unremagnetized and remagnetized limestones. *Journal of Geophysical Research*. 1994; 99: 4613–4623.
- [17] Jackson M. Diagenetic sources of stable remanence in remagnetized Paleozoic cratonic carbonates: a rock magnetic study. *Journal of Geophysical Research*. 1990; 95: 2753–2761.

- [18] Jackson M, Rochette P, Fillion G, Banerjee S, Marvin J. Rock magnetism of remagnetized Paleozoic carbonates: low-temperature behavior and susceptibility characteristics. *Journal of Geophysical Research*. 1993; 98: 6217–6225.
- [19] Kruiver PP, Dekkers MJ, Heslop D. Quantification of magnetic coercivity components by the analysis of acquisition curves of isothermal remanent magnetisation. *Earth and Planetary Science Letters*. 2001; 189: 269–276.
- [20] Lowrie W. Identification of ferromagnetic minerals in a rock by coercivity and unblocking temperature properties. *Geophysical Research Letters*. 1990; 17: 159–162.
- [21] Takagi H, Miwa S, Yokomizo Y, Nishijima K, Enjoji M, Mizuno T, Amano K. Estimation of the paleostress field from the 3-D orientation distribution of microcracks and their geothermal conditions in the Toki Granite, central Japan. *Journal of the Geological Society of Japan*. 2008; 114: 321–335.
- [22] Hoshi H, Nishimura N. Paleomagnetic results from andesite dikes in Toki, Gifu Prefecture: implications for dike emplacement and rotation. In: *Abstract of Japan Geoscience Union Meeting; 20–25 May 2012; SEM21-P12; Makuhari*. 2012.
- [23] Nakamura K. Volcanoes as possible indicators of tectonic stress orientation—principle and proposal. *Journal of Volcanology and Geothermal Research*. 1977; 2: 1–16.
- [24] Oikawa T, Mashima H, Tanase A, Ninomiya A, Umeda K. K-Ar age of high magnesium andesite dikes at the Toki River in Gifu Prefecture, central Japan. *Journal of the Geological Society of Japan*. 2006; 112: 616–619.
- [25] Danhara T, Iwano H. Determination of zeta values for fission-track age calibration using thermal neutron irradiation at the JRR-3 reactor of JAEA, Japan. *Journal of the Geological Society of Japan*. 2009; 115: 141–145.
- [26] Kinoshita O. Migration of igneous activities related to ridge subduction in Southwest Japan and the East Asian continental margin from the Mesozoic to the Paleogene. *Tectonophysics*. 1995; 245: 25–35.
- [27] Itoh Y, Uno K, Arato H. Seismic evidence of divergent rifting and subsequent deformation in the southern Japan Sea, and a Cenozoic tectonic synthesis of the eastern Eurasian margin. *Journal of Asian Earth Sciences*. 2006; 27: 933–942.
- [28] Itoh Y, Takemura K. Quaternary geomorphic trends within Southwest Japan: extensive wrench deformation related to transcurrent motions of the Median Tectonic Line. *Tectonophysics*. 1993; 227: 95–104.
- [29] Tokiwa T. Timing of dextral oblique subduction along the eastern margin of the Asian continent in the Late Cretaceous: evidence from the accretionary complex of the Shimanto Belt in the Kii Peninsula, Southwest Japan. *Island Arc*. 2009; 18: 306–319.